# Emergent Properties of Nanosensor Arrays: Applications for Monitoring IgG Affinity Distributions, Weakly Affined Hypermannosylation, and Colony Selection for Biomanufacturing

Nigel F. Reuel,[†] Brittany Grassbaugh,[†] Sebastian Kruss,[†] J. Zachary Mundy,[†] Cary Opel,[†] Adebola O. Ogunniyi,[†] Kamal Egodage,[‡] Ramon Wahl,[‡] Bernhard Helk,[‡] Jingqing Zhang,[†] Z. Ilke Kalcioglu,[§] Kevin Tvrdy,[†] Darin O. Bellisario,[⊥] Bin Mu,[†] Steven S. Blake,[†] Krystyn J. Van Vliet,[§,‖] J. Christopher Love,[†] Karl Dane Wittrup,[†,‖] and Michael S. Strano[†,*]

[†]Department of Chemical Engineering, Massachusetts Institute of Technology, Cambridge, Massachusetts 02139, United States, [‡]Technical Research and Development, BPRD, Novartis Pharma AG, Basel, Switzerland, [§]Department of Materials Science and Engineering, Massachusetts Institute of Technology, Cambridge, Massachusetts 02139, United States, [‖]Department of Biological Engineering, Massachusetts Institute of Technology, Cambridge, Massachusetts 02139, United States, and [⊥]Department of Chemistry, Massachusetts Institute of Technology, Cambridge, Massachusetts 02139, United States

ABSTRACT It is widely recognized that an array of addressable sensors can be multiplexed for the label-free detection of a library of analytes. However, such arrays have useful properties that emerge from the ensemble, even when monofunctionalized. As examples, we show that an array of nanosensors can estimate the mean and variance of the observed dissociation constant (K_D), using three different examples of binding IgG with Protein A as the recognition site, including polyclonal human IgG ($K_D \mu = 19 \mu M$, $\sigma^2 = 1000$ mM^2), murine IgG ($K_D \mu = 4.3$ nM, $\sigma^2 = 3 \mu M^2$), and human IgG from CHO cells ($K_D \mu = 2.5$ nM, $\sigma^2 =$

0.01 μM^2). Second, we show that an array of nanosensors can uniquely monitor weakly affined analyte interactions *via* the increased number of observed interactions. One application involves monitoring the metabolically induced hypermannosylation of human IgG from CHO using PSA-lectin conjugated sensor arrays where temporal glycosylation patterns are measured and compared. Finally, the array of sensors can also spatially map the local production of an analyte from cellular biosynthesis. As an example, we rank productivity of IgG-producing HEK colonies cultured directly on the array of nanosensors itself.
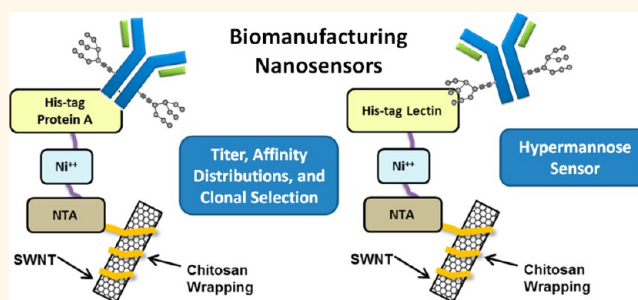
KEYWORDS: nanotube · sensor · array · biomanufacturing · glycan · affinity distribution

T he concept of vastly multiplexing analyte detection using arrays of independently addressable sensors is ubiquitous in the literature,[1,2] following successful demonstrations of the DNA[3,4] and protein[5,6] microarrays. This approach has been a prevailing motivation for further reduction in array size to nanometer dimensions.[7−9] Such nanosensor arrays, however, have other important capabilities that are not as well recognized, even when functionalized for just a single analyte. For example, many biological analytes, including antibodies, demonstrate a distribution of dissociation constants even in relatively

purified form.[10−12] In this work, we demonstrate that an array of sensors can reconstruct this important distribution *via* sampling a large number of independent interactions. Such arrays can also quantify weakly affined interactions by recording a large number of rare binding events. Lastly, a nanosensor array can also characterize and differentiate biosynthesis around single cells and colonies, enabling the label-free selection of more productive strains, as we are the first to show. These new properties have the potential to greatly enhance process analytics for biomanufacturing applications.

Improved analytical technology[13−15] for the rapidly increasing production of clinical recombinant antibodies[16−20] is an area of great interest. In fact, several recent studies highlight the need for improved (1) clonal selection,[21−23] (2) glycan analysis,[24−29] and (3) determining the affinity distribution or heterogeneity of the expressed product.[10−12] Cell line generation and selecting culture parameters typically take over a year with current assays[30] (the clonal selection part is ∼6 weeks but can also take multiple rounds to find the best candidate), and often cell candidates are only picked based on static measurements of productivity.[22,23] Glycosylation patterns can easily change due to processing conditions (media components,[31−33] temperature,[34] pH,[35] pCO_2,[36] dissolved oxygen,[37] cell density,[38] duration,[31] etc.), and they have a dramatic effect on the pharmacokinetics and immunogenicity of the resulting drug.[39,40] Current titer and glycosylation analytical technologies such as ELISA and tandem LC/MS systems, respectively, can deliver exquisite detail at the expense of much time and reagent. Furthermore, their processing steps are prohibitive to any online process use. The trend to milliliter-sized bioreactors[41] for upstream process optimization will also require platforms that can accurately assay much lower protein and glycan quantities. Finally, harsh biomanufacturing process conditions (pH, temperature, mixing) and variability in cell production result in heterogeneous products with a distribution of binding affinities, and currently, there is no convenient platform on which to measure the dissociation constant (K_D) distribution. Emerging nanoengineered sensors[42] fabricated in massive (10 000+ sites) arrays could provide solutions to these three areas of biomanufacturing analytics. We have previously described carbon-nanotube-based optical sensors for single protein[43] and single glycan[44] detection. However, in this work, our focus is instead on previously unacknowledged properties of nanosensor arrays, in general, as described above. We demonstrate completely new functions of such arrays for assaying binding heterogeneity, weakly affined hypermannosylation detection, and determining local cell productivity of biomanufactured products.

RESULTS AND DISCUSSION

Sensor Fabrication and Detection Method. Single-walled carbon nanotubes (SWNT) are arrayed (Figure 1a) in a porous (60−90 nm pore diameter) polyacrylamide hydrogel to reduce nonspecific binding[45,46] and allow for fast diffusion of the IgG analytes to the SWNT sensors (Figure 1b; Supplement 1a−d provides extensive material characterization of the SWNT gel platform). A basal gel with no SWNT is used on the glass substrate to position the thin sensor layer in a separate focal plane and eliminate the background fluorescence caused by glass impurities. The platform is excited by a 660 nm laser (Crystal Laser) on an inverted

microscope (Zeiss D.1), and the nIR emission is collected as an image stack on a 256 × 320 pixel InGaAs array (Princeton Instruments Acton Array). The SWNTs are suspended in chitosan and have been chemically modified as before[44] to display chelated nickel groups that act as both the docking site for His-tagged capture proteins (Protein A and PSA-lectin here) and as the signal transducer (proximity quencher). In brief, the nanotube acts as an optical switch, brightening as antibodies bind to the capture protein. The ensemble response of the array is created by averaging the intensity values over the entire array for each time point and is analogous to other bioassay techniques like ELISA and Biacore SPR measurements. Divalent nickel, Protein A, and IgG addition (100 mM, 1 mg/mL, 1.5 mg/mL) cause a decrease, increase, and additional increase, respectively (Figure 1c(i)). Subsequent washing of the gel surface shows negligible effects on the ensemble signal, which we interpret as absence of unbinding. Adding a BSA control (2 mg/mL) does not elicit a sensor response (Figure 1c(i)). Alternatively, the responses of all SWNT pixels can be monitored as histograms of percent modulation ($I_0 - I_{final}/I_0$) (Figure 1c(ii)). Sensor specificity can also be observed qualitatively with a nIR heat map filtered to the 10 000 most responsive sites (Figure 1d). To render the sensor array specific, we observed that the sensor protein (Protein A or PSA-lectin) must first be docked to the chelated nickel; otherwise, BSA can elicit a response (Supplement 2a). Although the ensemble response can be efficiently used to construct calibration curves and monitor titer and glycosylation trends, the averaging loses the valuable information about the affinity distribution recorded by each of the individual sensor elements.

Modeling a Nanosensor Array To Measure K_D Distributions. Consider an analyte with a Gaussian distribution of K_D and variance (σ_t^2) assayed on a 1 mm² total area array of otherwise independently addressable sensors. Obviously, as the total area is subdivided further and further into a population of independent sensor regions, the exact K_D distribution can be stochastically observed and recovered as the area of a single sensor approaches the projected area of the analyte. Before this limit is reached, however, if each sensor element reports an average of the interactions from multiple molecules, the measured sample variance (σ_m^2) is much smaller than the actual value (Figure 2a inset). For a Gaussian distribution of K_D, this decay of σ_m/σ_t scales as $1/N^{1/2}$ (Supplement 2b), where N is the number of molecules averaged on each sensor site (Figure 2a). This relation informs the effect of concentration and sensor area and identifies the regime where nanosensor arrays can effectively report on the variance of K_D (Figure 2b, assumes 10 nm² area for antibodies). Our demonstration platform in this work uses nanotubes arranged in 1.4 μm² pixels in
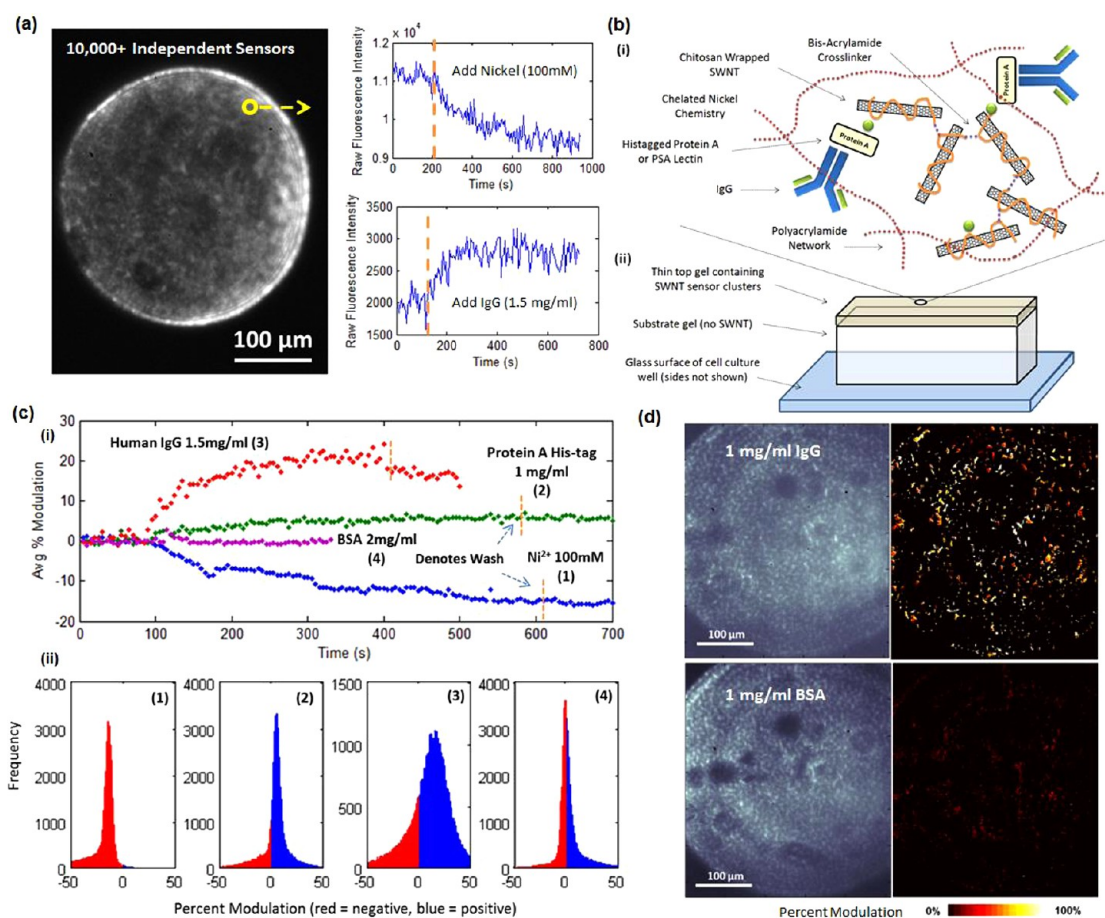
Figure 1. Nanosensor array fabrication and detection methods. (a) nIR micrograph of nanosensor array; each SWNT-illuminated pixel records changes in intensity upon analyte binding, such as nickel quenching or signal return from IgG adsorption shown. (b) Multilayer, polyacrylamide gel platform used to immobilize the SWNT sensors and provide a porous network for IgG diffusion. SWNT sensors are wrapped in chitosan, nickel-chelated, and functionalized with a capture protein (Protein A or PSA-lectin). (c) Ensemble (i) and all-points histogram (ii) response to 100 mM nickel (1), 1 mg/mL Protein A (2), 1.5 mg/mL human IgG (3), and 2 mg/mL BSA (4) additions. (d) Selectivity of the sensor array (nIR micrograph of starting intensities shown) as demonstrated by a heat map reporting the percent modulation response of the 10 000 top responding pixels after analyte addition.

the concentration ranges of nanomolar to micromolar, thus determining distributions of K_D among samples is feasible when the intrinsic variance of the sensor response is low.

A model is first needed to map our experimental array response back to an initial variance in binding. To simulate the array response, a more realistic distribution of K_D for an antibody is used. The Weibull distribution has been proposed for antibody affinity due to its ability to effectively present skewness in the probability distribution function using two shape parameters (α and β).[12] Antibody affinity is intuitively nonsymmetric as changes in the optimal protein will more often result in reduced binding and rarely enhance the product. Thus an antibody with positive skew in $\log_{10}(K_D)$ is modeled (tail with higher K_D values or analytes with less affinity), and the probability density function (PDF) is expressed as

$$\phi_1(x; \alpha, \beta) = \frac{\beta}{\alpha}\left(\frac{x}{\alpha}\right)^{\beta-1} e^{-(x/\alpha)^\beta} \quad \text{where } x = \log_{10}\left(\frac{1}{K_D}\right) \tag{1}$$

This distribution is initially centered at $K_D = 100$ nM (can be translated for other values) such that $\alpha = 7$ and β can vary from 2 to 45+ with 2 being a very large tail (high variance) and 45+ being an essentially monodisperse distribution (Figure 2c(i)). The sensor response is modeled by the Langmuir equation (eq 2) where the coverage fraction (θ_L) is determined by $1/K_D$ and sample concentration (C) (Figure 2c(ii)). In this case, θ_L represents the extent to which a nanotube sensor is turned on by a small number of local interacting molecules during the time of light acquisition (1s per frame).

$$\theta_L(\phi_1, C) = \frac{\left(\frac{1}{K_D}\right)C}{1 + \left(\frac{1}{K_D}\right)C} \quad \text{where } \left(\frac{1}{K_D}\right) \text{ is sampled from } \phi_1(x; \alpha, \beta) \tag{2}$$

Empirically, we find for our platform that the extent to which a nanotube sensor responds to adsorption is dictated by its starting intensity (I_0) and extent of functionalization (PF) which can be both experimentally measured and fit with another Weibull (φ_2) and Gaussian distribution (φ_3), respectively (Supplement 2c).
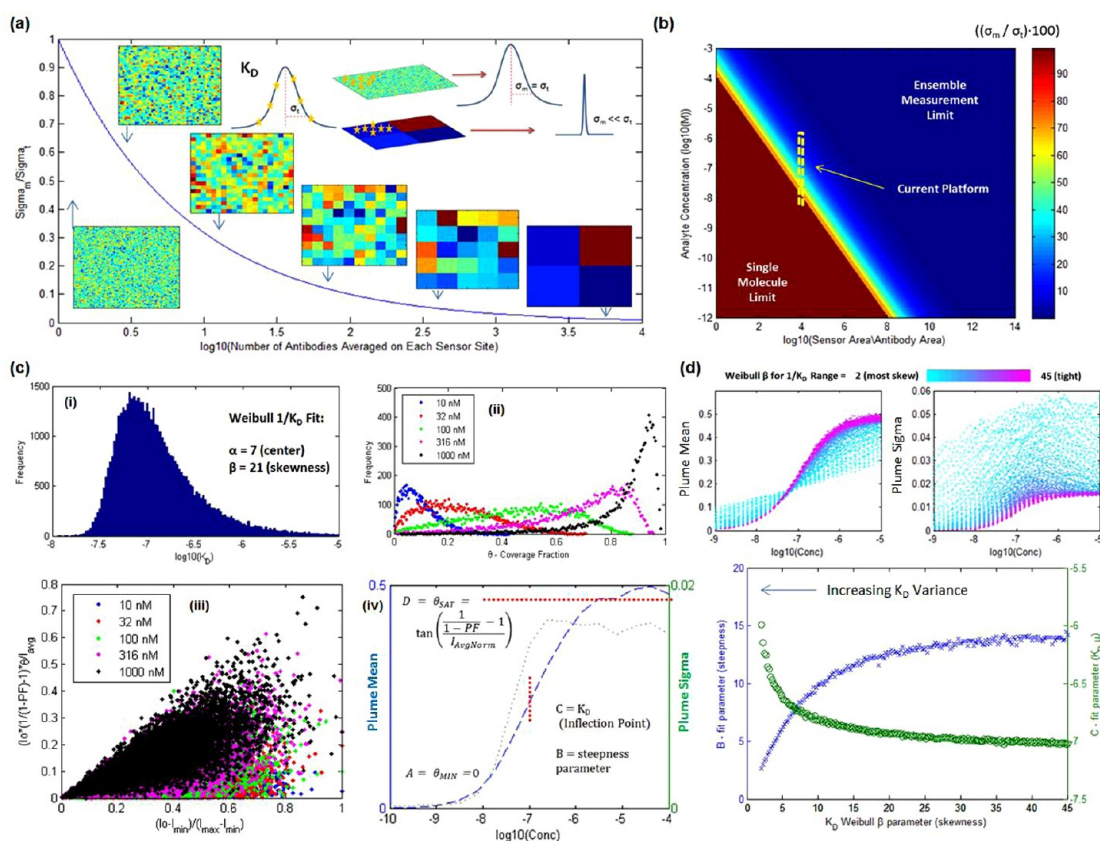
Figure 2. Modeling a nanosensor array for measuring K_D distributions. (a) Assuming a Gaussian shaped K_D distribution with known variance (σ_t^2), the effect of averaging number of molecules (N) on a single sensor site on measured variance (σ_m^2). (b) Design regime where σ_t^2 can be reconstructed showing two spectrum limits (ensemble and single molecule detection) and where our current nanosensor platform operates. (c) Modeling nanotube array response: (i) assuming a Weibull (skewed) K_D distribution, (ii) Langmuir coverage fraction to determine extent of nanosensor modulation, (iii) resulting simulated response "plume" normalized by average sensor intensity (I_{avg}) where each point represents a sensor site, and (iv) calibration curve from fitting the plume angle mean and standard deviation (θ_μ and θ_σ) with a bivariate Gaussian distribution. (d) Effect of changing K_D distribution skewness (β) on resulting θ_μ and θ_σ calibration curves as well as fit parameters "B" (steepness of calibration curve) and "C" (K_D mean).

It is important to note that the number of binding sites on the sensor protein is also imbedded in the functionalization variance (if all nanotubes were uniformly wrapped, functionalized, and had the same number of binding sites, this variable would be a constant). To stochastically simulate the response of an ensemble, for example, individual sensor responses, R, can be obtained as a coverage fraction, intensity, and percent functionalization value (θ, I_0, and PF), randomly generated from their respective PDFs (φ_1, φ_2, φ_3) and subsequently evaluated as

$$R(\theta_L(\phi_1, C), \phi_2(I_0), \phi_3(PF)) = \frac{I_0 \left(\frac{1}{1-PF} - 1 \right) \theta_L}{I_{avg}} \quad (3)$$

The response is normalized by the average intensity (I_{avg}) as each experimental platform's overall intensity may change due to variance in the experimental setup or quality of SWNT. This normalization allows for clear comparison of distinct arrays assayed at different concentrations. By plotting against the normalized starting intensity (($I_0 - I_{min})/(I_{max} - I_{min}$)), characteristic response "plumes" are observed (Figure 2c(iii)).

The modeled plumes are fit well by a bivariate Gaussian distribution in polar coordinates (θ,R), and the mean plume angle (θ_μ) is used to create the calibration curve (Figure 2c(iv)). The standard deviation in the plume angle (θ_σ) also has an interesting dependence on starting K_D skew (β) and is reported (Figure 2c(iv)). The θ_μ calibration curve is fit by a four-parameter logistics curve (used for many other bioassays that exhibit a signal saturation; i.e., ELISA); however, in this case, two parameters are known from experimental conditions ($A = \theta_{min} = 0$ and $D = \theta_{SAT} =$ eq 5).

$$\text{plume } \theta_\mu(x) = \left(\frac{A - D}{1 + \left(\frac{X}{C} \right)^B} \right) + D \text{ where } x = \log_{10}(C) \quad (4)$$

$$D = \theta_{SAT} = \tan\left(\frac{\frac{1}{1-PF} - 1}{I_{avgnorm}} \right) \quad (5)$$

The parameter B is a measure of steepness, and C is equal to the inflection point at K_D. By analyzing the
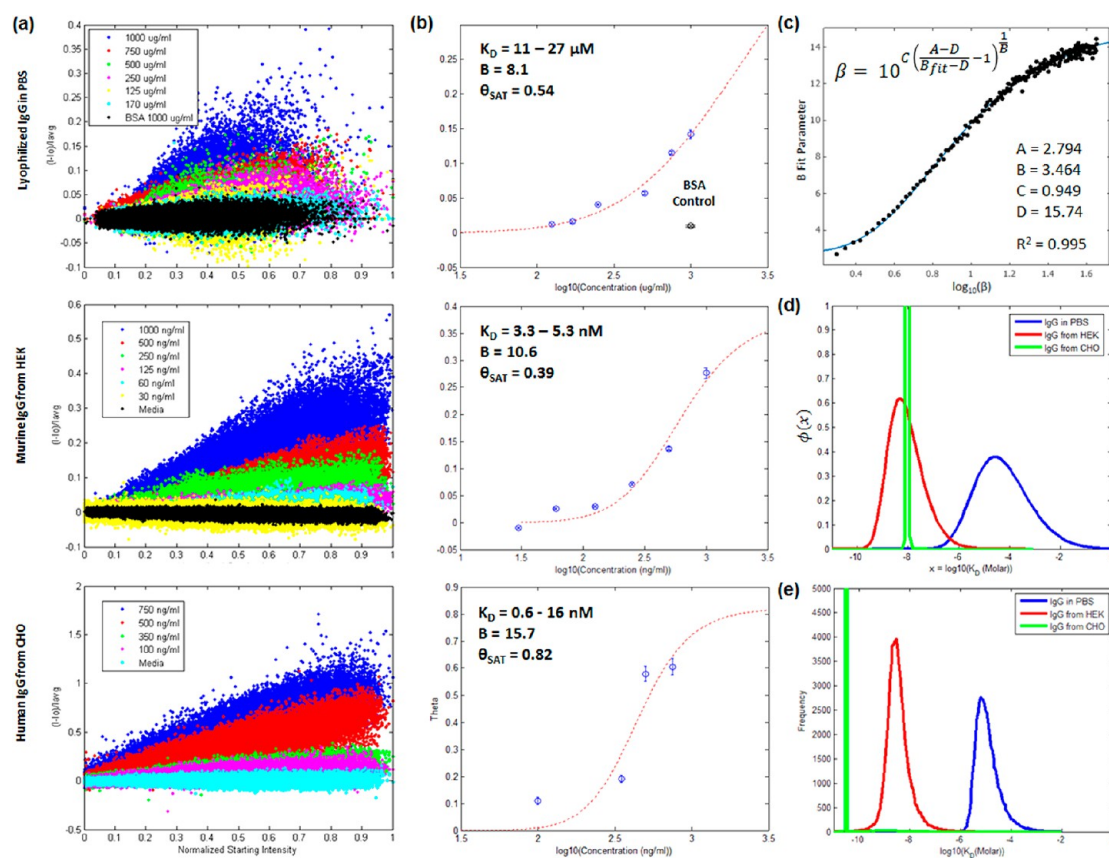
Figure 3. Experimental results from lyophilized IgG in PBS, murine IgG (TA99) from HEK cells, and human IgG from CHO cells screened on sensor arrays at various concentrations. (a) All-point sensor response plumes and fit calibration curves (b) yielding K_D 95% confidence intervals, B-fit parameters, and angle saturation values (θ_{SAT}) calculated from the starting intensity distribution of each sensor batch (eq 5). (c) Relation of B-fit parameter and K_D skewness parameter (β) as found by simulation results. (d) Measured K_D distributions using assumed Weibull PDF. (e) K_D histograms directly calculated from sensor response assuming a constant functionalization value, revealing the approximate shape of the true PDF.

model at many different extents of K_D skewness ($2 < \beta < 45$), the effect of K_D variance on the fit parameters was found (Figure 2d). As the distribution of antibody affinities becomes tighter (β increases), the nanosensor array yields a steeper calibration curve (Figure 3c fits this relation) (online Supplement 2d and 3c include a movie and simulation code).

K_D Distributions and Calibration Curves from Experimental Data. The array of nanotube sensors conjugated to His-tagged Protein A (Abcam) was used to assay three different samples of IgG with expected differences in affinity distributions: (1) commercial, lyophilized, poly-clonal human IgG reconstituted in PBS; (2) murine IgG (TA99) from an engineered human embryonic kidney (HEK) cell line; and (3) human IgG (b12) cultured from Chinese hamster ovary (CHO) cells (relevant controls in Supplement 2e). The data plumes predicted by the model were observed for each of the systems (Figure 3a), and the resulting calibration curves (Figure 3b) yielded K_D mean values (95% confidence intervals for each: $11-27\ \mu M$, $3.3-5.3$ nM, and $0.6-16$ nM) comparable to those found in literature for IgG–Protein A interactions ($2-50$ nM from SPR,[47] 34 nM from acoustic device[48]). The calibration curve also provided "B"-fit parameters

(eq 4) that are related to the starting distribution skew parameter (β) as solved from the model simulation (Figure 3c). With K_D mean (α) and skewness (β), the affinity PDF of each system (eq 1) can be determined (Figure 3d). As expected, the freshly expressed human IgG has the greatest affinity for Protein A with the least amount of variance. The murine antibody has a com-parable K_D average but much more predicted variance. This difference could be due to less efficient binding of murine IgG to Protein A as observed in the literature.[49] Finally, the lyophilized, polyclonal human IgG shows a $1000\times$ reduction in K_D and a much broader distribu-tion of affinities likely due to denaturation damage[50] or freeze–thaw cycles[51] (vs the freshly expressed CHO product). One limitation of the modeling approach is the a priori assumption of PDF form (in this case Weibull). The array of nanosensors can be used to report distributions directly, without any assumption of PDF form by calculating the Langmuir coverage from the response of each individual sensor (eqs 2 and 3) and creating a histogram of K_D values (Figure 3e). To do this now, however, one assumes a constant percent functionalization value (PF = 0.14, mean of ϕ_3) and chooses a concentration value away
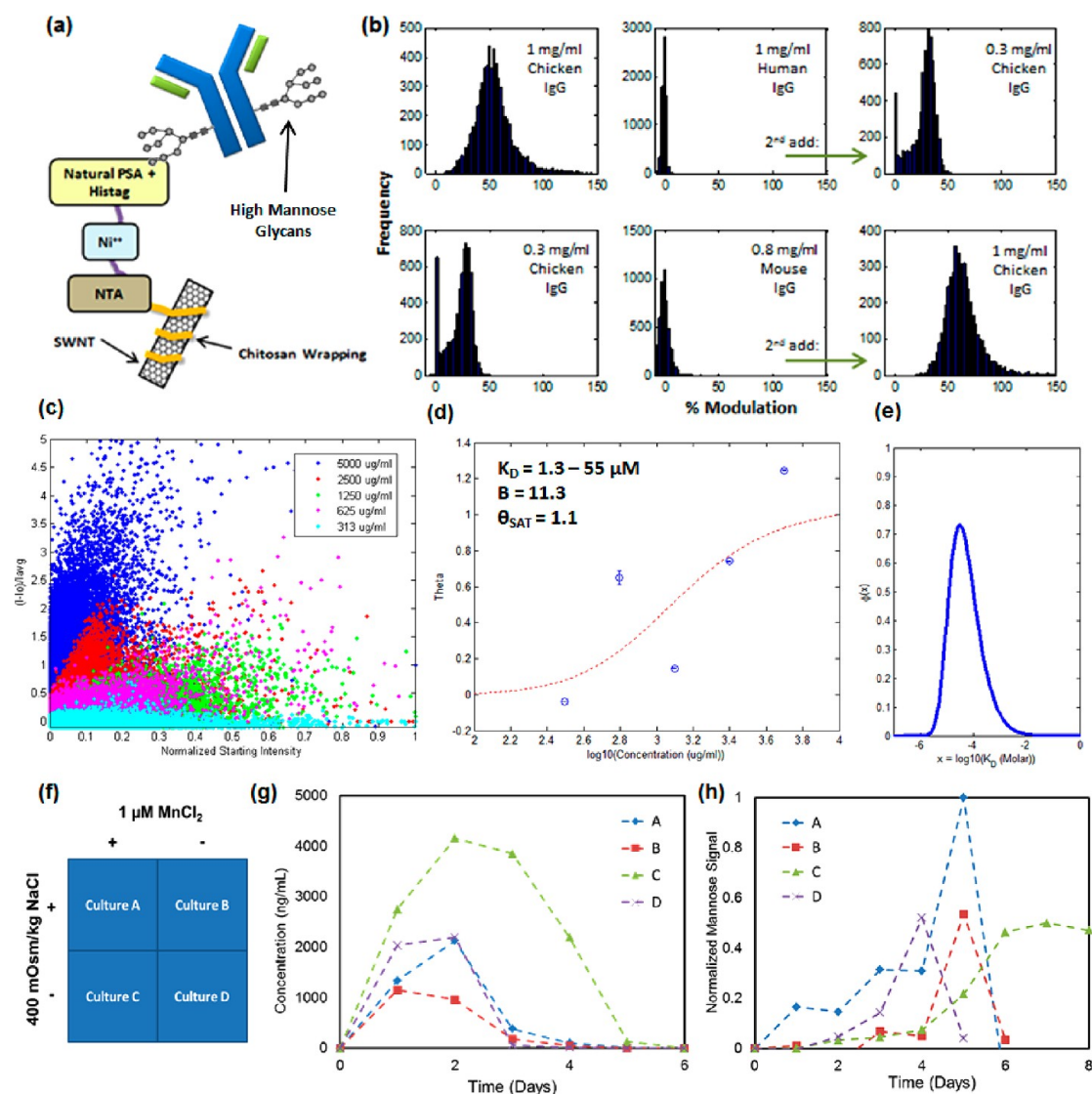
Figure 4. Hypermannosylation detection on PSA-lectin conjugated sensor arrays. (a) Weaker mannose-PSA-lectin interactions can be transduced on independent nanosensors. **(b)** Results of testing concept with chicken IgG which has >40% high mannose glycoforms where human and mouse IgG do not contain these isoforms. **(c)** All-point plume responses and calibration curve **(d)** as before with corresponding K_D distribution **(e)**. **(f)** Media compositions used to elicit hypermannosylation in CHO cell culture. Culture was sampled for 8 days showing expected changes in IgG titer from ELISA **(g)** and mannose content from SWNT sensor array **(h)**.

from saturation. These assumptions are an approximation as a distribution of functionalization (φ_3) exists, and each concentration does not align perfectly on the calibration curve, so each plume will yield a slightly different K_D histogram with differing K_D mean values (as can be seen with the CHO data, green trace, in Figure 3e). This direct technique for measurement can be improved by better fabrication methods, reducing the intrinsic variance of length and functionalization. We do note however that the direct reporting approach also presents K_D distributions with similar shape and positive skew as our model assumed.

Hypermannosylation Detection: Weakly Affined Interactions on Nanosensor Arrays. Another advantage of nanosensor arrays is their ability to report weak binding events—a greater number of individual sensor sites increases the

probability of a detection event, and this event is not averaged to null with other nonresponsive sites, as in the case for an ensemble sensor. The label-free nature of the platform is also beneficial to detecting weakly affined ligands since it requires no washing steps. By swapping out the His-tagged Protein A with a His-tagged, mannose-specific plant lectin, *Pisum sativum* agglutinin (PSA), the sensor platform can detect specifically high mannose content IgG (Figure 4a). Different species of IgG were initially used to test this concept. Chicken IgG contains an appreciable amount of glycoforms with high mannose content (>40% of population), whereas these are virtually absent in human and mouse IgG.[28] The SWNT sensor responses to human, mouse, and chicken IgG in PBS align with these findings and confirm that the platform can detect
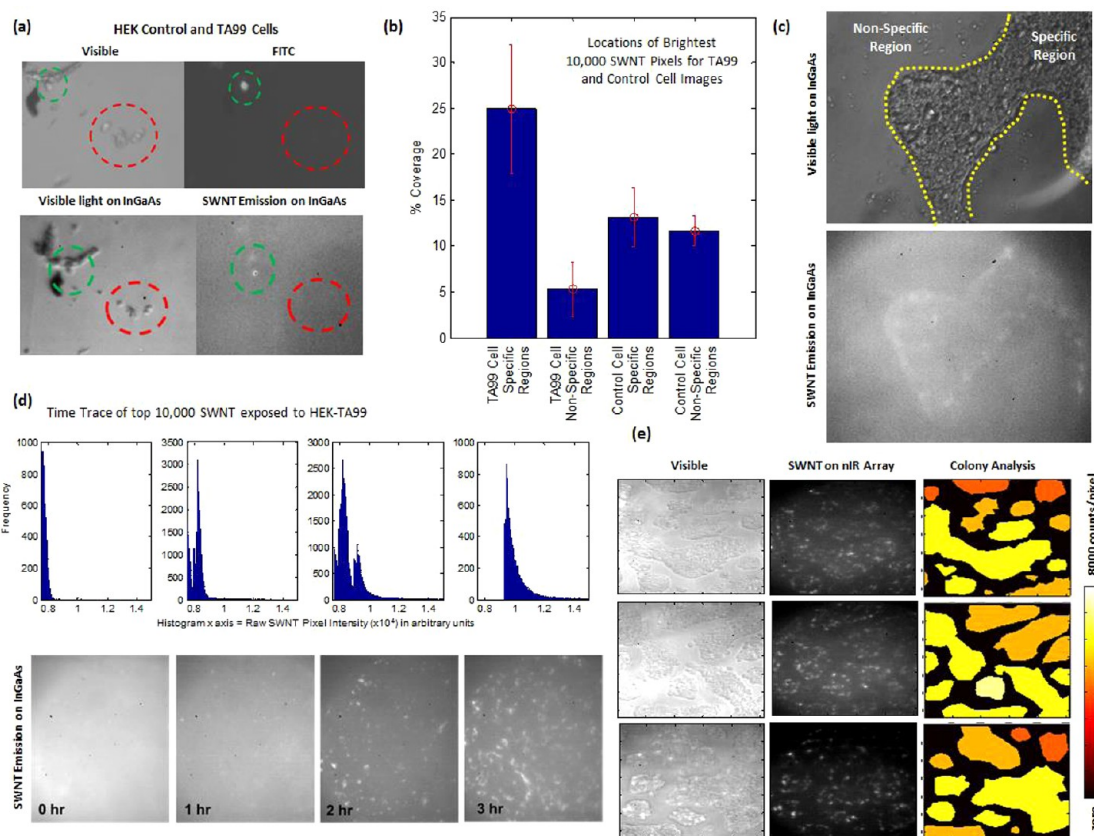
Figure 5. Sensor response to local HEK cell production. (a) Qualitative images of control and IgG-producing cells showing colocalization of SWNT response. (b) Location of top 1000 SWNTs in IgG and control cell images, presented as coverage percentage of cell area (specific) and gel area (nonspecific) in each image (c). (d) Dynamic response of SWNT sensors to IgG-producing cells plated on gel presented as distributions of top 1000 SWNTs from images and micrographs of scaled SWNT intensity. (e) Mapping visible IgG-producing cell islands, the colocalized SWNT signal underneath, and ranking the islands' productivity based on intensity normalized by island area.

mannose species with the PSA-lectin specifically (Figure 4b). A well-characterized sample of IgG with high mannose content from a fungal expression system (Novartis) was then used to further validate detection and obtain a calibration curve and K_D distribution as before (Figure 4c–e). The mannose IgG–PSA affinity ($K_D = 1.3$–55 μM 95% confidence interval) is comparable to literature values (μM > K_D > mM for lectin–glycan interactions[52]) with a broad distribution (Figure 4e). This is expected as 60% of the IgG sample is aglycosylated (verified by MS analysis) and the remaining 40% bear differing lengths and structures of high mannose-type glycans (verified by released glycan analysis; Novartis).

It has also been shown that changing culture conditions such as media components can affect the onset and extent of IgG hypermannosylation. In order to further validate our platform, we designed an experiment for CHO cultures in which levels of NaCl were increased and a MnCl$_2$ additive was used while monitoring mannose content over time using traditional peptide-N-glycosidase F release and capillary electrophoresis.[31] We cultured four identical dishes of CHO cells in which we fed media compositions derived from this study (Figure 4f). The supernatants were collected

after each 24 h period, diluted to a standardized 10 ng/mL IgG concentration, and assayed on our PSA-rendered sensor gels. The IgG concentrations were determined with ELISA (Figure 4g), and if below 10 ng/mL, the sample was run at stock concentration. The resulting trends (Figure 4h) determined by the mean percent modulation from the nanosensor array distributions (Supplement 2f) match those found in the previous study: (1) increased mannose content as culture time increases, (2) increased mannose from higher NaCl osmolality, and (3) delayed onset of hypermannosylation from MnCl$_2$ additive. The presence of mannose in these samples was confirmed by surface staining with fluorescently tagged PSA (Supplement 2g). We note that the sensitivity demonstrated by the array exceeded the capabilities of established glycan characterization tools; the same samples were captured on Protein A columns, cleaved, and interrogated using LC/MS, but there was not adequate signal to resolve glycosylated species (Novartis).

Nanosensor Arrays for Monitoring Local Cell Colony Production. A gel with an imbedded array of nanosensors can be used to screen local production of cells. Unfortunately, single cells are very difficult to culture for long
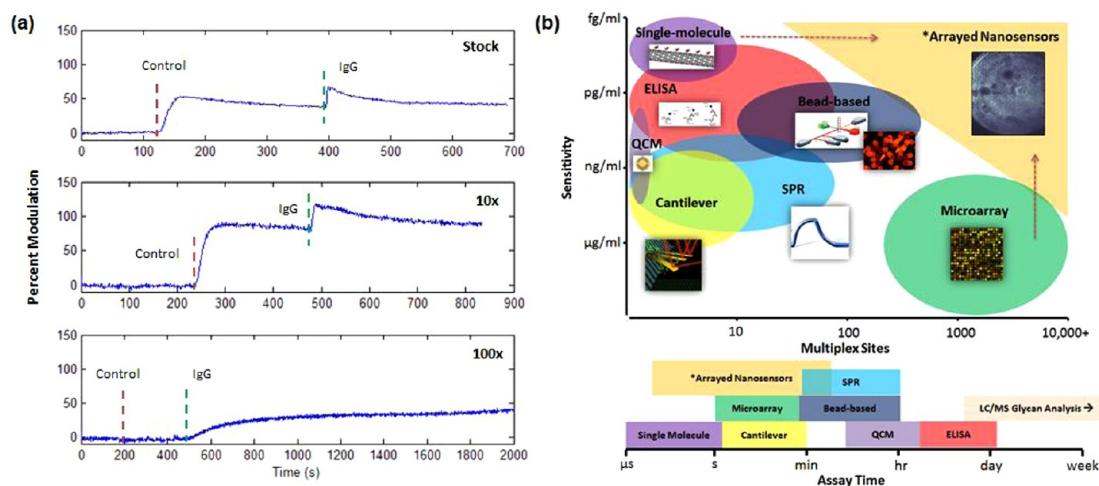
Figure 6. (a) Ensemble response of high concentration IgG bioreactor supernatant delivered from a fungal cell expression system assayed at different dilutions along with samples from the nontransfected cell line that was cultured in parallel, delivering a similar high background concentration of proteins. A 100× dilution is necessary to suppress background proteins from saturating the sensor array. (b) Experimental domain addressed by arrayed nanosensors in comparison to existing technologies. Also mapped are approximate assay times of each technique.

periods of time on the current porous platform (little indications of healthy, single cell adherence). The single cells that did culture well, however, displayed colocalization of IgG production on a Protein A-incubated gel (Figure 5a). By seeding a greater number of cells, larger colonies of cells formed on the porous gel surface and were able to produce for longer time periods (24 h). By analyzing images of control and IgG-producing HEK cell islands after 24 h of production, we observed a statistical difference between the two profiles of production. By ranking the brightest 1000 SWNTs and then querying their location, there is a greater localization of the bright SWNT under IgG-producing islands, whereas they are evenly or randomly distributed within and outside of the control cell islands (Figure 5b,c; code in Supplement 3b). We then plated HEK cells producing IgG on a gel and acquired multiple images of the nIR intensities at 0, 1, 2, and 3 h. Histograms of the 1000 brightest SWNT pixels in these images show a "turn-on" trend that is likely due to IgG production (Figure 5d). Finally, large HEK islands of HEK cells were allowed to grow overnight on a Protein A gel. The nIR response was clearly colocalized under each of the islands, and the response was summed, averaged over the island area, and each island was ranked based on productivity (Figure 5e).

CONCLUSION

Here we have reported on carbon-nanotube-based fluorescent sensor arrays for monitoring distributions of K_D, hypermannosylation, and local cellular production of IgG with clear implications in biomanufacturing. The platform was demonstrated with lyophilized IgG in PBS as well as characterizing freshly expressed IgG in complex media from three different cellular expression systems: HEK, CHO, and a fungal cell line. The sensor

array was rendered specific to mannose with PSA-lectin, and trends in metabolically induced hypermannosylation from a previous study were confirmed. Finally, local production of IgG from HEK cell colonies cultured on sensor arrays was monitored. Better upstream colony selection could be performed with a sensor gel optimized for healthy cell culture. The cell colonies could be exposed to various culture and media conditions, and their productivity and glycosylation patterns could be monitored in real time. This platform could lead to more rapid and informed selection of master cell lines and culture conditions based on multiple parameters rather than picking colonies based on static snapshots of productivity provided by current assays.[23] During production, sensor arrays in a microfluidic platform could monitor product titer, K_D distribution, and glycosylation by periodically sampling the bioreactor, filtering cellular components, diluting to a set level depending on the cell line's average productivity (Figure 6a), read the fluorescent signal, and then regenerate for the next sample. We have demonstrated that the Protein A gels can be regenerated using a pH 3.0 release wash, similar to regeneration of Protein A purification columns with little loss of sensitivity (Supplement 2h). Detection of mannose has been validated here, but other glycans of interest (galactose, fucose, sialic acids, and non-human, immunogenic glycans like gal-α 1,3-gal[53]) could also be detected by multiplexing portions of the nanosensor array with different His-tag lectins. The longstanding goal of nanosensor arrays is to preserve the sensitivity and analytical advantages of single-molecule nanosensors with the multiplexing ability of macroscale techniques, thus filling an untapped analytical regime (Figure 6b). The fast assay time (<5 min) of nanosensor arrays could also provide a disruptive[54]

alternative to the more time-intensive ELISA and LC/MS analytics that are currently used (Figure 6b). The current limitations of these arrays are the intrinsic variances caused by nonautomated production in small batches (16−32 gels per batch). Small variations in polymer casting time, initiator concentration, and washing procedures result in gels with varying levels of functionalization and sensitivity. A standardized gel from an automated printing/production system could reduce this variance and provide a robust tool for biomanufacturing analytics and beyond.

METHODS

SWNT Sensor and Gel Platform Fabrication. SWNTs were suspended in chitosan as before.[44] In brief, 3 mg of purified HiPCO SWNT (Unidym) was added to 20 mL of chistosan suspension (0.25 wt % in water containing 1 vol % acetic acid; Sigma). The resulting mixture was tip sonicated (1/4 in. tip Cole Parmer, model CV18) at 10 W for 45 min in an ice bath and table-top centrifuged three times at 13.2 rpm for 90 min each, while collecting the suspended SWNT supernatant and discarding the aggregate pellet after each cycle. The SWNT was then mixed at a 50:50 volume ratio with the polyacrylamide mixture for casting as the top layer. The amount of monomer (acrylamide) and cross-linker (N,N′-methylenebisacrylamide; both Sigma) was specified using standard %T %C nomenclature where %T refers to the overall weight % of polymer (monomer and cross-linker) in the solution and %C refers to the weight % of the total polymer that is cross-linker. The optimal surface gel was found to be 3%T and 1%C. A substrate gel (6%T 1%C) was also prepared. TEMED (tetramethylethylenediamine) was added in at 0.7 vol % in both the top and bottom gel solutions to stabilize the radical reaction. A fresh initiator solution of 1 wt % ammonium persulfate (APS) was made immediately prior to each gel batch. The APS, bottom and top gel solutions, and substrate chips (8 chamber Lab-Tek by Nunc) were degassed in the glovebox antechamber to remove absorbed and dissolved oxygen. Within the nitrogen-controlled glovebox (MBraun LABstar), 1 vol % of the APS solution was added to the substrate gel to initiate the polymerization, and it was immediately cast (100 μL to each well) and then allowed to cure for 1 h. The top gel was then initiated with 1 vol % APS and immediately spotted at 20 μL to each gel surface and allowed to cure for 1 h.

The functionalization steps of the chitosan-wrapped SWNT were also similar to those of our previous work.[44] In brief, the amine groups of the chitosan were reacted with succinic anhydride (133 mM in PBS 7.4 buffer; Sigma) overnight and then washed thoroughly with water. The carboxylic acid functional groups were then activated with 100 mM EDC and 520 mM NHS (Sigma) in MES buffer pH 4.7 (Pierce) for 2 h. After being washed with water thoroughly, the gels were then reacted with 34 mM $N\alpha,N\alpha$-bis(carboxymethyl)-L-lysine hydrate (Sigma) in PBS 7.4 buffer overnight. The gels were then washed and incubated with a 100 mM nickel sulfate solution for 20 min. These chips were then washed thoroughly in water and stored in water.

Poroelastic Relaxation Indentation and Dextran Release Curves. The gel pore size was evaluated by AFM-enabled indentation as described previously.[55] In brief, an AFM silicon cantilever with a polystyrene sphere of 45 μm diameter (Novascan) was used to acquire load relaxation data as force vs time (Asylum Research, MFP3D). Data were acquired for multiple sites on each gel type (Supplement 1b). This was done repeatedly for multiple sites on each gel type. A custom Matlab algorithm was then used to analyze the load relaxation responses and to determine the average pore diameter (Supplement 3b).

FITC-conjugated dextran particles (Invitrogen) of various sizes (10, 40, 70, and 500 kDa) were also absorbed into 150 μL cylindrical gel plugs over 48 h. The impregnated gels were then removed, washed, and inserted into clean water. The release of the FITC particles was observed by sampling the exterior fluid and assaying the FITC content with a plate reader. Using standard curves, the release can then be presented as cumulative mass release over time (Supplement 1b).

Data Collection on nIR Inverted Microscope. The SWNT sensor data presented in this paper were collected on a custom inverted microscope (Zeiss D.1 Observer) that was fitted with a 660 nm laser (Crystal Laser, 100 mW). A 20× planar objective (Zeiss) was used, and the emission intensities were recorded by a nitrogen-cooled InGaAs array (Princeton Instruments). Win Spec software (Princeton Instruments) was used to collect the SWNT emission and saved as an image stack TIF file. This file was then analyzed using the Matlab code presented in Supplement 3. Analyte samples were added to the sensor gels by hand, applying the 100 μL sample to the lower right corner of the well as not to place the plastic pipet tip in the laser beam path.

To prepare a sensor gel for testing, it was first thoroughly washed with PBS to exchange the buffer and then allowed to incubate with the His-tag sensor protein (Protein A (Abcam) or PSA-lectin (Vector Laboratories; conjugated to His-tag peptide (Abbiotec) via Traut's reagent and SMCC linker (Pierce)) at 500 μg/mL overnight. The gel was again washed thoroughly with PBS and then fitted on the microscope for testing.

HEK Cell Line Generation and CHO Origin. A tricistronic expression cassette pLB2-CMV-GFP-TA99 was created using 2A skip peptides.[56] The light and heavy chain sequences of TA99, a murine IgG2a antibody,[57] were linked by a T2A sequence. The expression cassette was cloned into the lentiviral vector, pLB2,[58] modified with a CMV promoter driving GFP-F2A expression, creating the complete plasmid sequence of pLB2-CMV-GFP-F2A-LC-T2A-HC. All cloning was performed using overlap extension PCR. HEK-GFP-TA99 cells were generated using a modified version of a previously described protocol.[59] Briefly, HEK-293FT cells (Invitrogen) were transfected with the following plasmids: pLB2-CMV-GFP-TA99, pCMV-dR8.91,[60] and pCMV-VSV-G[61] at a mass ratio of 2:1:1 using PEI. After 24 h, fresh medium was exchanged. Then, 48 and 72 h later, supernatant containing lentiviral particles was harvested. HEK-293 cells were transduced twice for 24 h by incubation with freshly harvested supernatant supplemented with protamine sulfate at 5 μg/mL. GFP-positive cells were selected to a purity of greater than 95% using flow fluorescence activated cell sorting at the Koch Institute flow cytometry core.

The CHO cell line has been cultured by the Love et al. group as received (courtesy of D. Burton, Scripps Research Institute). Details on the generation of this cell line can be found in the following paper.[62]

Cell Passaging and Culture. For standard culture, the media used were DMEM (with 4.5 g/L glucose, 10% heat inactivated FBS (Invitrogen), 2 mM L-glutamine, 100 U/mL penicillin, 100 U/mL streptomycin; rest Sigma) and GMEM (same additives; Sigma) for the HEK and CHO cultures, respectively. For cultures used in experiments, a serum-free medium was used for growth and as a buffer in the sensor gel (Invitrogen Freestyle 293). To passage the cells, they were allowed to grow to confluence, washed with PBS, and then released with Trypsin (0.05% w/0.53 mM EDTA). The cells were then pelleted, resuspended in fresh media, and diluted at a 1:5 ratio. The cells were passaged every 2−3 days and discarded after the 20th passage.

Hypermannosylation CHO Culture Experiment. CHO cells were seeded at equal density in small culture flasks (25 cm²; Sarstedt) and allowed to grow to confluence with regular GMEM media (overnight). The growth medium was then exchanged with 3 mL of serum-free media (Freestyle 293 Invitrogen), and the cells were allowed to produce for 24 h. The medium was then saved, and a fresh 3 mL of serum-free medium was added for the next 24 h cycle. This was repeated for 10 days. The IgG

content was measured by ELISA (ICL Lab, Inc.), and the samples were diluted to 10 ng/mL in Freestyle to run on the PSA-incubated SWNT gels.

REFERENCES AND NOTES

1. Kingsmore, S. F. Multiplexed Protein Measurement: Technologies and Applications of Protein and Antibody Arrays. *Nat. Rev. Drug Discovery* **2006**, *5*, 310–320.
2. Nielsen, U. B.; Geierstanger, B. H. Multiplexed Sandwich Assays in Microarray Format. *J. Immunol. Methods* **2004**, *290*, 107–120.
3. Epstein, J. R.; Biran, I.; Walt, D. R. Fluorescence-Based Nucleic Acid Detection and Microarrays. *Anal. Chim. Acta* **2002**, *469*, 3–36.
4. Cheng, M. M. C.; Cuda, G.; Bunimovich, Y. L.; Gaspari, M.; Heath, J. R.; Hill, H. D.; Mirkin, C. A.; Nijdam, A. J.; Terracciano, R.; Thundat, T.; *et al.* Nanotechnologies for Biomolecular Detection and Medical Diagnostics. *Curr. Opin. Chem. Biol.* **2006**, *10*, 11–19.
5. Schweitzer, B.; Kingsmore, S. F. Measuring Proteins on Microarrays. *Curr. Opin. Biotechnol.* **2002**, *13*, 14–19.
6. Wilson, D. S.; Nock, S. Recent Developments in Protein Microarray Technology. *Angew. Chem., Int. Ed.* **2003**, *42*, 494–500.
7. Niemeyer, C. M. Functional Devices from DNA and Proteins. *Nano Today* **2007**, *2*, 42–52.
8. Tam, J. M.; Song, L.; Walt, D. R. DNA Detection on Ultrahigh-Density Optical Fiber-Based Nanoarrays. *Biosens. Bioelectron.* **2009**, *24*, 2488–2493.
9. Tan, C. P.; Cipriany, B. R.; Lin, D. M.; Craighead, H. G. Nanoscale Resolution, Multicomponent Biomolecular Arrays Generated by Aligned Printing with Parylene Peel-Off. *Nano Lett.* **2010**, *10*, 719–725.
10. Werblin, T. P.; Siskind, G. W. Distribution of Antibody Affinities: Technique of Measurement. *Immunochemistry* **1972**, *9*, 987.
11. Pierson, L.; Allauzen, S.; Blumenthal, M.; Rosenberg, A. An Automated Method for Determination of Antibody Affinity Distribution Functions with Nanogram Quantities. *J. Immunol. Methods* **1998**, *211*, 97–109.
12. Steensgaard, J.; Steward, M. W.; Frich, J. R. The Significance of Antibody-Affinity Heterogeneity in Antigen-Antibody Reactions Demonstrated by Computer-Simulation. *Mol. Immunol.* **1980**, *17*, 689–698.
13. Henriques, J. G.; Buziol, S.; Stocker, E.; Voogd, A.; Menezes, J. C. Monitoring Mammalian Cell Cultivations for Monoclonal Antibody Production Using Near-Infrared Spectroscopy. In *Optical Sensor Systems in Biotechnology*; Rao, G., Ed.; Springer-Verlag: Berlin, 2009; Vol. 116, pp 73−97.
14. Pizarro, S. A.; Dinges, R.; Adams, R.; Sanchez, A.; Winter, C. Biomanufacturing Process Analytical Technology (PAT) Application for Downstream Processing: Using Dissolved Oxygen as an Indicator of Product Quality for a Protein Refolding Reaction. *Biotechnol. Bioeng.* **2009**, *104*, 340–351.
15. Rodrigues, M. E.; Costa, A. R.; Henriques, M.; Azeredo, J.; Oliveira, R. Technological Progresses in Monoclonal Antibody Production Systems. *Biotechnol. Prog.* **2010**, *26*, 332–351.
16. Holliger, P.; Hudson, P. J. Engineered Antibody Fragments and the Rise of Single Domains. *Nat. Biotechnol.* **2005**, *23*, 1126–1136.
17. Butler, M. Animal Cell Cultures: Recent Achievements and Perspectives in the Production of Biopharmaceuticals. *Appl. Microbiol. Biotechnol.* **2005**, *68*, 283–291.
18. Farid, S. S. Process Economics of Industrial Monoclonal Antibody Manufacture. *J. Chromatogr., B* **2007**, *848*, 8–18.
19. Glennie, M. J.; van de Winkel, J. G. J. Renaissance of Cancer Therapeutic Antibodies. *Drug Discovery Today* **2003**, *8*, 503–510.
20. Adams, G. P.; Weiner, L. M. Monoclonal Antibody Therapy of Cancer. *Nat. Biotechnol.* **2005**, *23*, 1147–1157.
21. Hacker, D. L.; De Jesus, M.; Wurm, F. M. 25 Years of Recombinant Proteins from Reactor-Grown Cells—Where Do We Go from Here?. *Biotechnol. Adv.* **2009**, *27*, 1023–1027.
22. Browne, S. M.; Al-Rubeai, M. Selection Methods for High-Producing Mammalian Cell Lines. *Trends Biotechnol.* **2007**, *25*, 425–432.
23. Burke, J. F.; Mann, C. J.; Jiang, S.; Klottrup, K. J.; Smithers, N.; Ahmed, O. Using ClonePix FL To Assess Monoclonality. *Genet. Eng. Biotechnol. News* **2009**, *29*, 38–39.
24. Elliott, S.; Lorenzini, T.; Asher, S.; Aoki, K.; Brankow, D.; Buck, L.; Busse, L.; Chang, D.; Fuller, J.; Grant, J.; *et al.* Enhancement of Therapeutic Protein *In Vivo* Activities through Glycoengineering. *Nat. Biotechnol.* **2003**, *21*, 414–421.
25. Hermeling, S.; Crommelin, D. J. A.; Schellekens, H.; Jiskoot, W. Structure−Immunogenicity Relationships of Therapeutic Proteins. *Pharm. Res.* **2004**, *21*, 897–903.
26. Jefferis, R. Glycosylation of Recombinant Antibody Therapeutics. *Biotechnol. Prog.* **2005**, *21*, 11–16.
27. Jefferis, R. Glycosylation as a Strategy To Improve Antibody-Based Therapeutics. *Nat. Rev. Drug Discovery* **2009**, *8*, 226–234.
28. Raju, T. S.; Briggs, J. B.; Borge, S. M.; Jones, A. J. S. Species-Specific Variation in Glycosylation of IgG: Evidence for the Species-Specific Sialylation and Branch-Specific Galactosylation and Importance for Engineering Recombinant Glycoprotein Therapeutics. *Glycobiology* **2000**, *10*, 477–486.
29. van Berkel, P. H. C.; Gerritsen, J.; Perdok, G.; Valbjorn, J.; Vink, T.; van de Winkel, J. G. J.; Parren, P. N-Linked Glycosylation Is an Important Parameter for Optimal Selection of Cell Lines Producing Biopharmaceutical Human IgG. *Biotechnol. Prog.* **2009**, *25*, 244–251.
30. Wurm, F. M. Production of Recombinant Protein Therapeutics in Cultivated Mammalian Cells. *Nat. Biotechnol.* **2004**, *22*, 1393–1398.
31. Pacis, E.; Yu, M.; Autsen, J.; Bayer, R.; Li, F. Effects of Cell Culture Conditions on Antibody N-Linked Glycosylation: What Affects High Mannose 5 Glycoform. *Biotechnol. Bioeng.* **2011**, *108*, 2348–2358.
32. Gramer, M. J.; Eckblad, J. J.; Donahue, R.; Brown, J.; Shultz, C.; Vickerman, K.; Priem, P.; van den Bremer, E. T. J.; Gerritsen, J.; van Berkel, P. H. C. Modulation of Antibody Galactosylation through Feeding of Uridine, Manganese Chloride, and Galactose. *Biotechnol. Bioeng.* **2011**, *108*, 1591–1602.
33. Lee, S. Y.; Kwon, Y. B.; Cho, J. M.; Park, K. H.; Chang, S. J.; Kim, D. I. Effect of Process Change from Perfusion to Fed-Batch on Product Comparability for Biosimilar Monoclonal Antibody. *Process Biochem.* **2012**, *47*, 1411–1418.
34. Ahn, W. S.; Jeon, J. J.; Jeong, Y. R.; Lee, S. J.; Yoon, S. K. Effect of Culture Temperature on Erythropoietin Production and Glycosylation in a Perfusion Culture of Recombinant CHO Cells. *Biotechnol. Bioeng.* **2008**, *101*, 1234–1244.
35. Muthing, J.; Kemminer, S. E.; Conradt, H. S.; Sagi, D.; Nimtz, M.; Karst, U.; Peter-Katalinic, J. Effects of Buffering Conditions and Culture pH on Production Rates and Glycosylation of Clinical Phase I Anti-Melanoma Mouse IgG3 Monoclonal Antibody R24. *Biotechnol. Bioeng.* **2003**, *83*, 321–334.
36. Schmelzer, A. E.; Miller, W. M. Hyperosmotic Stress and Elevated pCO(2) Alter Monoclonal Antibody Charge Distribution and Monosaccharide Content. *Biotechnol. Prog.* **2002**, *18*, 346–353.
37. Serrato, J. A.; Palomares, L. A.; Meneses-Acosta, A.; Ramirez, O. T. Heterogeneous Conditions in Dissolved Oxygen Affect N-Glycosylation but Not Productivity of a Monoclonal Antibody in Hybridoma Cultures. *Biotechnol. Bioeng.* **2004**, *88*, 176–188.

38. Majid, F. A. A.; Butler, M.; Al-Rubeai, M. Glycosylation of an Immunoglobulin Produced from a Murine Hybridoma Cell Line: The Effect of Culture Mode and the Anti-apoptotic Gene, bcl-2. *Biotechnol. Bioeng.* **2007**, *97*, 156–169.

39. Bumbaca, D.; Boswell, C. A.; Fielder, P. J.; Khawli, L. A. Physiochemical and Biochemical Factors Influencing the Pharmacokinetics of Antibody Therapeutics. *AAPS J.* **2012**, *14*, 554–558.

40. Goetze, A. M.; Liu, Y. D.; Zhang, Z. Q.; Shah, B.; Lee, E.; Bondarenko, P. V.; Flynn, G. C. High-Mannose Glycans on the Fc Region of Therapeutic IgG Antibodies Increase Serum Clearance in Humans. *Glycobiology* **2011**, *21*, 949–959.

41. Lee, K. S.; Boccazzi, P.; Sinskey, A. J.; Ram, R. J. Microfluidic Chemostat and Turbidostat with Flow Rate, Oxygen, and Temperature Control for Dynamic Continuous Culture. *Lab Chip* **2011**, *11*, 1730–1739.

42. Reuel, N. F.; Mu, B.; Zhang, J.; Hinckley, A.; Strano, M. S. Nanoengineered Glycan Sensors Enabling Native Glyco-profiling for Medicinal Applications: Towards Profiling Glycoproteins without Labeling or Liberation Steps. *Chem. Soc. Rev.* **2012**, *41*, 5744–5779.

43. Ahn, J. H.; Kim, J. H.; Reuel, N. F.; Barone, P. W.; Boghossian, A. A.; Zhang, J. Q.; Yoon, H.; Chang, A. C.; Hilmer, A. J.; Strano, M. S. Label-Free, Single Protein Detection on a Near-Infrared Fluorescent Single-Walled Carbon Nanotube/Protein Microarray Fabricated by Cell-Free Synthesis. *Nano Lett.* **2011**, *11*, 2743–2752.

44. Reuel, N. F.; Ahn, J. H.; Kim, J. H.; Zhang, J. Q.; Boghossian, A. A.; Mahal, L. K.; Strano, M. S. Transduction of Glycan-Lectin Binding Using Near-Infrared Fluorescent Single-Walled Carbon Nanotubes for Glycan Profiling. *J. Am. Chem. Soc.* **2011**, *133*, 17923–17933.

45. Ruchel, R.; Steere, R. L.; Erbe, E. F. Transmission-Electron Microscopic Observations of Freeze-Etched Polyacryla-mide Gels. *J. Chromatogr.* **1978**, *166*, 563–575.

46. Wang, J.; Gonzalez, A. D.; Ugaz, V. M. Tailoring Bulk Transport in Hydrogels through Control of Polydispersity in the Nanoscale Pore Size Distribution. *Adv. Mater.* **2008**, *20*, 4482–4489.

47. Nohldén, S. Affinity Determination of Protein A Domains to IgG Subclasses by Surface Plasmon Resonance. Ph.D. Thesis, Linköpings Universitet, Linköping, 2008.

48. Saha, K.; Bender, F.; Gizeli, E. Comparative Study of IgG Binding to Proteins G and A: Nonequilibrium Kinetic and Binding Constant Determination with the Acoustic Wave-guide Device. *Anal. Chem.* **2003**, *75*, 835–842.

49. Richman, D. D.; Cleveland, P. H.; Oxman, M. N.; Johnson, K. M. The Binding of Staphylococcal Protein-A by the Sera of Different Animal Species. *J. Immunol.* **1982**, *128*, 2300–2305.

50. Schersch, K.; Betz, O.; Garidel, P.; Muehlau, S.; Bassarab, S.; Winter, G. Systematic Investigation of the Effect of Lyo-philizate Collapse on Pharmaceutically Relevant Proteins I: Stability after Freeze-Drying. *J. Pharm. Sci.* **2010**, *99*, 2256–2278.

51. Burry, R. W. *Immunocytochemistry—A Practical Guide for Biomedical Research*; Springer: Berlin, 2010; pp 7−16.

52. Hirabayashi, J. Concept, Strategy and Realization of Lectin-Based Glycan Profiling. *J. Biochem.* **2008**, *144*, 139–147.

53. Chung, C. H.; Mirakhur, B.; Chan, E.; Le, Q.; Berlin, J.; Morse, M.; Murphy, B. A.; Satinover, S. M.; Hosen, J.; Mauro, D.; *et al.* Cetuximab-Induced Anaphylaxis and IgE Specific for Ga-lactose-α-1,3-galactose. *N. Engl. J. Med.* **2008**, *358*, 1109–1117.

54. Bower, J. L.; Christensen, C. M. Disruptive Technologies—Catching the Wave. *Harvard Bus. Rev.* **1995**, *73*, 43–53.

55. Kalcioglu, Z. I.; Mahmoodian, R.; Hu, Y. H.; Suo, Z. G.; Van Vliet, K. J. From Macro- to Microscale Poroelastic Charac-terization of Polymeric Hydrogels *via* Indentation. *Soft Matter* **2012**, *8*, 3393–3398.

56. Hu, T.; Fu, Q.; Chen, P.; Zhang, K.; Guo, D. Y. Generation of a Stable Mammalian Cell Line for Simultaneous Expression of Multiple Genes by Using 2A Peptide-Based Lentiviral Vector. *Biotechnol. Lett.* **2009**, *31*, 353–359.

57. Thomson, T. M.; Mattes, M. J.; Roux, L.; Old, L. J.; Lloyd, K. O. Pigmentation-Associated Glycoprotein of Human Mela-nomas and Melanocytes: Definition with a Mouse Mono-clonal-Antibody. *J. Invest. Dermatol.* **1985**, *85*, 169–174.

58. Stern, P.; Astrof, S.; Erkeland, S. J.; Schustak, J.; Sharp, P. A.; Hynes, R. O. A System for Cre-Regulated RNA Interference *in Vivo*. *Proc. Natl. Acad. Sci. U.S.A.* **2008**, *105*, 13895–13900.

59. Kuroda, H.; Kutner, R. H.; Bazan, N. G.; Reiser, J. Simplified Lentivirus Vector Production in Protein-Free Media Using Polyethylenimine-Mediated Transfection. *J. Virol. Methods* **2009**, *157*, 113–121.

60. Zufferey, R.; Nagy, D.; Mandel, R. J.; Naldini, L.; Trono, D. Multiply Attenuated Lentiviral Vector Achieves Efficient Gene Delivery *in Vivo*. *Nat. Biotechnol.* **1997**, *15*, 871–875.

61. Dull, T.; Zufferey, R.; Kelly, M.; Mandel, R. J.; Nguyen, M.; Trono, D.; Naldini, L. A Third-Generation Lentivirus Vector with a Conditional Packaging System. *J. Virol.* **1998**, *72*, 8463–8471.

62. Hezareh, M.; Hessell, A. J.; Jensen, R. C.; van de Winkel, J. G. J.; Parren, P. Effector Function Activities of a Panel of Mutants of a Broadly Neutralizing Antibody Against Hu-man Immunodeficiency Virus Type 1. *J. Virol.* **2001**, *75*, 12161–12168.